The Astrophysical Journal, 804:12 (15pp), 2015 April 20 doi:10.1088/0004-637X/804/1/12

SPECTRAL EVOLUTION OF ANOMALOUS COSMIC RAYS AT *VOYAGER* 1 BEYOND THE TERMINATION SHOCK

U. K. Senanayake[1,2], V. Florinski[1], A. C. Cummings[3], and E. C. Stone[3]
[1] Department of Space Science and Center for Space Plasma and Aeronomic Research, University of Alabama in Huntsville, Huntsville, AL 35899, USA; uks0001@uah.edu, vaf0001@uah.edu
[2] Physics Department, University of Alabama in Huntsville, Huntsville, AL 35899, USA
[3] California Institute of Technology, Mail Code 290-17, Pasadena CA 91125, USA; ace@srl.caltech.edu, ecs@srl.caltech.edu
Received 2014 December 6; accepted 2015 February 24; published 2015 April 23

ABSTRACT

When the *Voyager 1* spacecraft crossed the termination shock (TS) on 2004 December 16, the energy spectra of anomalous cosmic rays (ACRs) could not have been produced by steady-state diffusive shock acceleration. However, over the next few years, in the declining phase of the solar cycle, the spectra began to evolve into the expected power-law profile. Observations at the shock led to a broad range of alternative theories for ACR acceleration. In spite of that, in this work we show that the observations could be explained by assuming ACRs are accelerated at the TS. In this paper, we propose that the solar cycle had an important effect on the unrolling of the spectra in the heliosheath. To investigate the spectral evolution of ACRs, a magnetohydrodynamic background model with stationary solar-wind inner boundary conditions was used to model the transport of helium and oxygen ions. We used a backward-in-time stochastic integration technique where phase-space trajectories are integrated until the so-called "injection energy" is reached. Our simulation results were compared with *Voyager 1* observations using three different diffusion models. It is shown that the spectral evolution of ACRs in the heliosheath at *Voyager 1* could be explained by an increase in the source strength and an enhancement in diffusion as a result of a decrease of the turbulent correlation length in the declining phase of the solar cycle. At the same time, drift effects seem to have had a smaller effect on the evolution of the spectra.

Key words: acceleration of particles – diffusion – shock waves – solar wind – Sun: heliosphere

1. INTRODUCTION

The *Voyager 1* (*V1*) and *Voyager 2* (*V2*) space probes, launched in 1977, are the farthest traveled human-made objects to date. Originally designed to explore the gas giant planets, the *Voyagers* continued their journey into the outer heliosphere and out of the solar system. At the time of this writing, *V1* and *V2* are at distances of 129 and 106 AU from the Sun, respectively. The cosmic ray subsystem (CRS) instrument on board the spacecraft detects cosmic ray nuclei from hydrogen through iron over an energy range of ∼1–500 MeV n^{-1} (Stone et al. 1977). In this work we are interested in the lower energy cosmic rays between 1 and 100 MeV n^{-1} known as anomalous cosmic rays (ACRs). ACRs were traditionally thought to be accelerated at the termination shock (TS) by diffusive shock acceleration (DSA; Krymskii 1977; Bell 1978; Blandford & Ostriker 1978; Pesses et al. 1981).

As was expected, the ACR intensities grew steadily prior to the shock crossing (e.g., Cummings et al. 2002). However, when *V1* crossed the TS in 2004 December at 94 AU, the spectrum was not consistent with theoretical predictions based on steady, first-order Fermi acceleration (Stone et al. 2005). Lower energy ACRs were at much lower levels than the expected source intensity. Subsequently, the spectra began to evolve as *V1* traveled deeper into the heliosheath (the region between the TS and the heliopause (HP), the magnetic boundary of the solar system). Over the next three years after the shock crossing, the intensity of 12–22 MeV n^{-1} anomalous He at *V1* increased by a factor of ∼21. Although intermediate-energy ACR intensities were higher as a result of the declining solar activity, similar spectra were observed at the *V2* TS crossing in 2007 September (Stone et al. 2008). As a result of the unexpected observations, alternative acceleration mechanisms were proposed, including source regions along the flanks and the tail (McComas & Schwadron 2006; Kóta & Jokipii 2008; Guo et al. 2010; Kóta 2010; Senanayake & Florinski 2013), magnetic reconnection near the HP (Lazarian & Opher 2009; Drake et al. 2010), and a pump mechanism that is mostly effective near the HP (Fisk & Gloeckler 2009). In 2012 August, heliospheric ions, including ACRs, have disappeared at *V1* and have not been observed since (Krimigis et al. 2013; Stone et al. 2013; Webber & McDonald 2013). That event was later confirmed to be a crossing of the heliospheric boundary (Gurnett et al. 2013).

In this work we consider *V1* observations in early 2005 (one month after the TS crossing) and in early 2012 (seven months before the HP). Solar cycle 23 reached its maximum in 2001, and the cycle 23/24 minimum was in 2008 (http://solarscience.msfc.nasa.gov/predict.shtml). The Sun remained quiescent until 2010, which marked the beginning of the weak solar cycle 24 (Jian et al. 2011; Russell et al. 2013). Solar wind takes about a year to reach the TS, and the conditions at *V1* in 2005 were only ∼40% of the maximum solar activity. By 2012 January, *V1* was near the HP, where the solar-wind time delay is about 4–5 yr (Zank & Müller 2003). Consequently, one would expect minimum solar activity at *V1* in 2012.

During the period from 2005 to 2012, the polarity of the heliospheric magnetic field remained negative ($A < 0$), causing positively charged particles to drift along the TS from high to low latitudes and toward the Sun along the heliospheric current sheet (HCS). Near the solar maximum, the tilt angle is large, and consequently, the particles' transport along the warped HCS is less efficient. Furthermore, the magnetic field is weaker during the solar minimum compared to the maximum (see Jian et al. 2011 for example). Another important factor

that affects transport is the spectrum of interplanetary magnetic turbulence. Magnetic field fluctuations (δB) are expected to be small during quiet solar minimum conditions in comparison to the maximum. Because we are primarily interested in investigating the rigidity dependence of the diffusion coefficient, we neglect the variations of B and δB over a solar cycle. Higher energy particles that resonate with fluctuations in the energy range of the turbulent spectrum have steeper rigidity-dependent diffusion coefficients compared to the lower energy particles that interact with inertial-range fluctuations (le Roux et al. 2007; le Roux 2011). The correlation length corresponds, approximately, to the outer scale of the turbulence, i.e., the transition between the energy and inertial ranges. Wicks et al. (2009, 2010) showed that the correlation length of magnetic field fluctuations is larger during solar maximum than at solar minimum. Because of the decrease in the turbulent correlation length with declining solar activity, lower energy particles will move into the energy range, yielding a steeper rigidity dependence of the diffusion coefficient.

Senanayake & Florinski (2013) examined ACR acceleration along a nonspherical TS using a semianalytical model for the plasma and magnetic field backgrounds. They found that the tail region of the TS was the preferred acceleration site for these particles, provided the perpendicular diffusion coefficient in the heliosheath was very small. Similar conclusions were earlier reached by McComas & Schwadron (2006), Kóta & Jokipii (2008), Guo et al. (2010), and Kóta (2010). All of these papers were either based on a flat current sheet model or did not include the HCS at all. In addition, none of them discussed the effects of the solar cycle on energetic particles accelerated on the tail part of the TS and transported to *Voyager* along the field lines. The results of Senanayake & Florinski (2013) were generally in a qualitative agreement with the *V1* observations, but did not match them on the quantitative level.

In this paper, we investigate the evolution of ACR spectra during the $A < 0$ solar cycle along the *V1* direction at the TS and in the heliosheath, taking into account the solar cycle effects such as changes in the HCS tilt angle, the diffusion coefficients, and the ACR source intensity. Three different diffusion models were used to explain the *V1* observations (see below). We employed a magnetohydrodynamic (MHD) plasma background with constant solar-wind inner boundary conditions. Particle simulations were performed for singly ionized helium and oxygen ions. A stochastic cosmic-ray transport was used, similar to our previous work (Senanayake & Florinski 2013).

The rest of the paper is organized as follows. The next section gives a brief description of the plasma background and the particle transport model. Section 3 describes the methods that were used to estimate the rigidity dependence of the diffusion coefficient. In Section 4 our simulation results are compared with *V1* CRS observations. The results are discussed and summarized in Section 5.

2. PLASMA BACKGROUND AND TRANSPORT MODEL

A global three-dimensional MHD model with a single population of neutral hydrogen was used to obtain the plasma background of the entire heliosphere and the nearby local interstellar medium (LISM). All simulations were performed on a geodesic grid (see Florinski et al. 2013 for the description of the plasma model). A level-six geodesic grid with 512 radial points was used, with the inner boundary at $r_0 = 5$ AU and the outer boundary at 900 AU. The simulation cell size in the radial direction was 0.4 AU between the inner boundary and 140 AU, and gradually increasing with radial distance afterward. The standard global heliospheric coordinate system was used, where the positive z axis is aligned with the solar rotation axis (Beck & Giles 2005), the negative x axis is a projection of the interstellar helium flow vector (Lallement et al. 2005) onto the heliographic equator, and the y axis completes the right-handed coordinate system. The LISM velocity was 23.2 km s^{-1} (McComas et al. 2012), and the LISM magnetic field was taken to be 4 μG in magnitude and directed at 32°.6 to the LISM flow vector in the hydrogen deflection plane formed by the interstellar helium and hydrogen velocity vectors. The LISM flow was assumed to have a proton density of 0.04 cm^{-3}, a neutral hydrogen density of 0.2 cm^{-3}, and temperatures of each component equal to 6,300 K.

The following conditions were imposed at 1 AU: density 4.07 cm^{-3}, radial velocity 581 km s^{-1}, and temperature 3.412×10^5 K. These values were then extended to 5 AU using the standard polytropic solution for the solar wind (Parker 1960). The plasma velocities measured by the *ACE* (http://www.srl.caltech.edu/ACE/ASC/level2/index.html) and *Ulysses* (Ebert et al. 2009) spacecraft in early 2004 were ~(500–650) km s^{-1}; we used a value that is close to the average during this time. The magnetic field was a Parker spiral (Parker 1958) with a radial component of 37.5 μG at 1 AU. The above parameter set resembles solar activity in the beginning of 2004 in the inner heliosphere (beginning of 2005 at *V1*). The TS is located at 90 AU in the *V1* direction, which is close to the actual distance (94 AU) during the shock encounter in late 2004. However, the distance to the HP in the model was much larger (~160 AU) in the same direction. This is a known problem with today's global models of the heliosphere (Pogorelov et al. 2004; Opher et al. 2006; Borovikov et al. 2011). For simplicity we assumed that the plasma background remained unchanged during the period of time covered by the ACR simulations.

In this work, we used the HCS tilt $\alpha = 55°$ to represent a period near the solar maximum and a flat current sheet for the solar minimum. The surface of the current sheet was traced kinematically after performing the MHD simulation with a unipolar magnetic field to maintain accuracy in the regions that contain the HCS. This was done by following streamlines backward in time until the inner boundary was reached. Points mapped above the location of the magnetic neutral line received the negative, or inward, polarity, and points below the positive, or outward, polarity, as appropriate for the $A < 0$ magnetic polarity cycle. The latitude of the magnetic equator Θ', given the azimuthal angle ϕ, was computed as (Pogorelov et al. 2007)

$$\Theta' = \sin^{-1}\left[\frac{\sin\alpha\sin\phi}{|\cos\phi|\left(\cos^2\alpha + \tan^2\phi\right)^{1/2}}\right], \quad (1)$$

where $\phi = \phi_0 + \Omega(t_{\rm trace} - t_{\rm sim})$, ϕ_0 is the azimuthal angle of the trace end point at the inner boundary, Ω is the angular velocity of solar rotation, $t_{\rm sim}$ is the total MHD simulation time, and $t_{\rm trace}$ is the advection time for the trace to reach the inner boundary from a given cell center.

Figure 1 shows the magnitude of the drift velocity in the meridional plane for the two values of the HCS tilt angles used

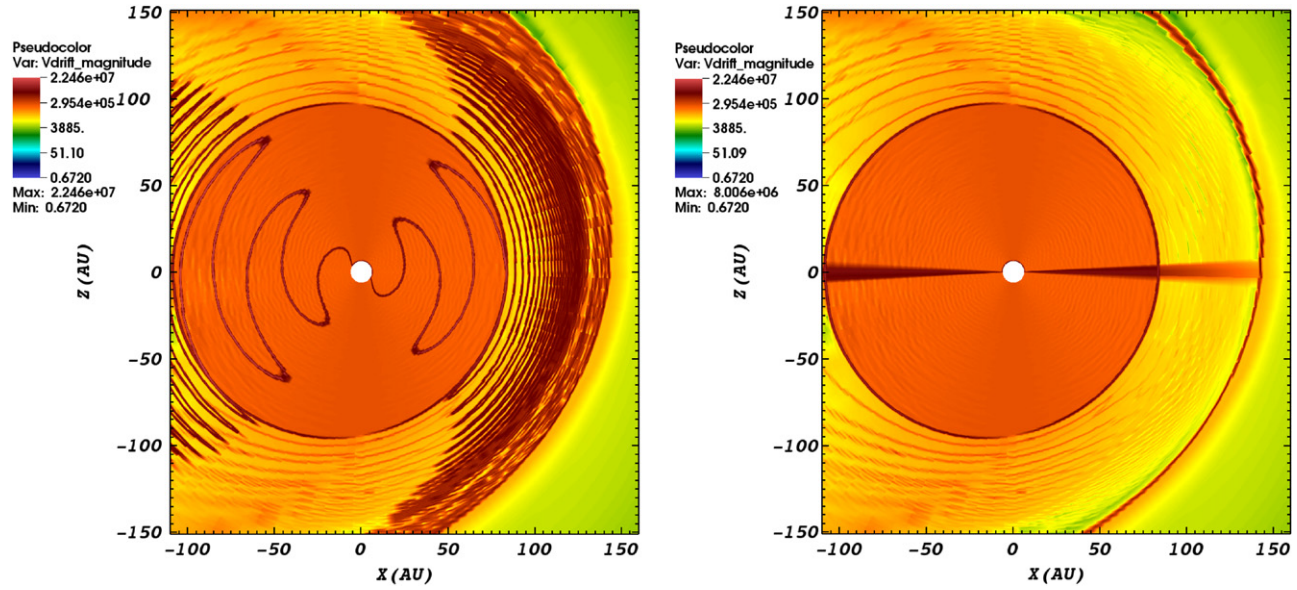

Figure 1. Left panel: drift velocity magnitude in the meridional plane for the HCS tilt angle $\alpha = 55°$. Here the solar rotation rate was reduced by a factor of 5 (see the text for details). Right panel: the same for a flat HCS, using the actual solar rotation rate.

in our simulations, $\alpha = 55°$ (left panel) and $\alpha = 0$ (right panel). Note that to resolve the sector structure in the heliosheath (for the tilted HCS), Ω had to be reduced by a factor of 5 (only at the HCS tracing stage; the magnetic field itself was calculated with the correct Ω). We can estimate the effect of this reduction by performing two otherwise identical simulations with Ω and $\Omega/5$, but not including drift effects in the heliosheath where the HCS cannot be reliably traced if the actual solar rotation rate is used. The resulting ACR spectra in the equatorial plane were then compared. We found that a reduction of the drift coefficient by a factor of 2 in the simulation with slower rotation resulted in a good agreement with the reference results. This reduction factor is used throughout this paper.

The ACR transport model is based on Parker's transport equation (Parker 1965), often written in the form of a backward Fokker–Planck equation, convenient for the method of solution using stochastic differential equations:

$$\frac{\partial f}{\partial t} + \left(u_i + v_{d,i} - \frac{\partial \kappa_{ij}}{\partial x_j}\right)\frac{\partial f}{\partial x_i} - \kappa_{ij}\frac{\partial^2 f}{\partial x_i \partial x_j} - \frac{\boldsymbol{\nabla}.\boldsymbol{u}}{3}\frac{\partial f}{\partial \ln p} = 0, \quad (2)$$

where f is the pitch-angle-averaged phase-space density, $\boldsymbol{u}$ is the plasma velocity, κ_{ij} is the diffusion tensor, and $v_{d,i}$ is the drift velocity. The diffusion coefficient in the fixed frame is given by

$$\kappa_{ij} = \kappa_\perp \delta_{ij} + (\kappa_\parallel - \kappa_\perp)\frac{B_i B_j}{B^2}, \quad (3)$$

where $\kappa_\parallel$ is the parallel diffusion coefficient, and $\kappa_\perp$ is the perpendicular diffusion coefficient.

We integrate Equation (2) along the phase-space trajectories backward in time until the injection energy (0.5 MeV n^{-1}) is reached, similar to Senanayake & Florinski (2013). The displacement of a trajectory in the solar rest frame is computed as in Florinski & Pogorelov (2009). The deterministic part of the displacement (during time dt) $dx_i^{\rm det}$ and the logarithmic momentum step $d \ln p$ are given by

$$dx_i^{\rm det} = -\left(u_i + v_{d,i} - \frac{\partial \kappa_{ij}}{\partial x_j}\right)dt, \quad (4)$$

$$d \ln p = \frac{\boldsymbol{\nabla}.\boldsymbol{u}}{3}dt. \quad (5)$$

The probabilistic (or stochastic) displacement is

$$dx_i^{\rm prob} = b_{ij}(x_i, t)dW_j(t), \quad (6)$$

where $b_{ij}(x_i, t)$ is a known tensor, and $dW_j(t)$ is an increment of the Wiener process (Gaussian random walk). The diffusive part was transformed into the field-aligned frame, where the diffusion tensor is diagonal. In that frame, Equation (6) reads

$$dx_i^{\rm prob} = Z(n_z)2\sqrt{\kappa_\parallel dt}\; b_i + R(n_r)2\sqrt{\kappa_\perp dt}\; c_i(n_\phi), \quad (7)$$

with normalized displacements $Z = \mathrm{erf}^{-1}(2n_z - 1)$ (along the mean field) and $R = \sqrt{\ln\left(1 - n_r\right)}$ (in the plane perpendicular to the mean field). In Equation (7), b_i and c_i are in the directions of parallel and perpendicular transport, and n_r, n_z, and n_ϕ are uniformly distributed random numbers between 0 and 1. The total displacement is given by $dx_i = dx_i^{\rm det} + dx_i^{\rm prob}$.

We chose diffusion coefficients assuming that the rigidity dependence of the diffusion coefficient changes for particles with energy greater than some characteristic energy (see Section 3). Two different expressions for the diffusion coefficients were used in this paper. For the first, we adapted the diffusion model from our previous work (Senanayake &

Table 1
Parameters in Model Fits in Figures 6–10

Period	Figure	Prior[a] Sunspot Number	Diffusion Model	κ_{0i} (cm^2s^{-1})	γ_1/γ_2	E_0 (He/O) (MeV n^{-1})	HCS Tilt	Injection Region	Injection Rate	χ^2		Acceptable Fit?	
										He	O	He	O
2005	6	~45	1	6.24×10^{22}	0.66/1.4	12/4	55°	polar	1	3.5	3.7	✓	✓
2005	6	~45	1	6.24×10^{22}	0.66/1.4	12/4	55°	nose	1	693	21	…	…
2005	8	~45	2	3.54×10^{24}	0.66/1.4	12/4	55°	uniform	1	3.4	3.3	✓	✓
2005	10	~45	3	3.84×10^{24}	0.7/1.47	50.7/3.25	55°	uniform	1	3.7	3.6	✓	✓
2012	7	~0	1	2.90×10^{23}	1.4	…	0°	polar	4	3.0	21	✓	…
2012	7	~0	1	2.90×10^{23}	1.4	…	55°	polar	4	2.4	34	✓	…
2012	7	~0	1	2.90×10^{23}	0.66/1.4	12/4	55°	polar	4	22	136	…	…
2012	9	~0	2	1.65×10^{25}	1.4	…	0°	uniform	8	2.7	20	✓	…
2012	9	~0	2	1.65×10^{25}	1.4	…	55°	uniform	8	2.0	27	✓	…
2012	9	~0	2	1.65×10^{25}	0.66/1.4	12/4	55°	uniform	8	6.5	35	…	…

Note.
[a] 2005: nine months earlier, 2012: four years earlier.

Florinski 2013) as follows:

$$\kappa_{\parallel 1} = \begin{cases} \kappa_{01} \dfrac{w}{c} \left(\dfrac{P}{P_0} \right)^{\gamma_1} \dfrac{B_0}{B} & ; E \leqslant E_0 \\ \kappa_{01} \dfrac{w}{c} \left(\dfrac{P_{E_0}}{P_0} \right)^{\gamma_1} \left(\dfrac{P}{P_{E_0}} \right)^{\gamma_2} \dfrac{B_0}{B} & ; E \geqslant E_0 \end{cases} \quad (8)$$

$$\kappa_{\perp 1} = a_1 \kappa_{\parallel 1}, \quad (9)$$

where $B_0 = 37.5$ μG is the magnetic field at 1 AU, w is the particle speed, P is the rigidity of the particle, $P_0 = 1$ GV, E is the particle's energy per nucleon, E_0 is the energy per nucleon where the rigidity dependence changes, P_{E_0} is the rigidity at E_0, $a_1 = 0.01$, γ_1 and γ_2 are chosen by comparing the *V1* anomalous helium and oxygen data at the TS and in the heliosheath (see below), and κ_{01} is a constant given below (see Table 1).

In the second method, the choice of parallel diffusion coefficient was motivated by quasi-linear theory (QLT; Jokipii 1966, 1971), where it depends on the spectrum of turbulent magnetic fluctuations. The turbulent magnetic field variance $\langle \delta B^2 \rangle$ was assumed to be proportional to the solar-wind plasma density upstream of the TS and $\langle \delta B^2 \rangle \sim B^2$ along the streamlines extending from the TS into the heliosheath, similar to Florinski & Pogorelov (2009). As a result, the ratio $B^2/\langle \delta B^2 \rangle$ does not vary with the radial distance r in the heliosheath and also in regions upstream of the TS where $B \sim 1/r$. However, in QLT $\kappa \propto w(P/B)^{\gamma}(B^2/\langle \delta B^2 \rangle)$, and therefore one would expect κ to vary with r everywhere.

The perpendicular diffusion coefficient was taken to be proportional to $\kappa_{\parallel}$ times the total (slab plus two-dimensional) magnetic variance (le Roux et al. 1999):

$$\kappa_{\parallel 2} = \begin{cases} \kappa_{02} \dfrac{w}{c} \left(\dfrac{P}{P_0} \right)^{\gamma_1} \dfrac{B^2}{\langle \delta B^2 \rangle} & ; E \leqslant E_0 \\ \kappa_{02} \dfrac{w}{c} \left(\dfrac{P_{E_0}}{P_0} \right)^{\gamma_1} \left(\dfrac{P}{P_{E_0}} \right)^{\gamma_2} \dfrac{B^2}{\langle \delta B^2 \rangle} & ; E \geqslant E_0 \end{cases} \quad (10)$$

$$\kappa_{\perp 2} = a_2 \kappa_{\parallel 2} \frac{\langle \delta B^2 \rangle}{B^2}, \quad (11)$$

where κ_{02} is a constant (see Table 1), and a_2 is a constant chosen to be 0.01 in the solar-wind region and 10^{-4} in the heliosheath. We used the standard expression for the drift velocity $v_{d,i}$, multiplied by the drift reduction coefficient, if required.

3. METHODS TO ESTIMATE THE RIGIDITY DEPENDENCE OF THE DIFFUSION COEFFICIENT

In this section, we will discuss two techniques that were used to estimate the rigidity dependence of the diffusion coefficient (γ). The first method is the more conventional approach used by most authors. The possibility of separating an anomalous spectrum into two components at the TS crossing will be discussed in this method. The second method is a new technique, which assumes that the entire ACR spectrum is a single component and that the changes in rigidity dependence of the diffusion coefficient (from γ_1 to γ_2) occur at the same rigidity (or gyroradius) for the species. From QLT, this gyroradius is close to the wavelength of slab turbulence at the break point in the power spectrum (l_b). Once the above rigidity value is found, it is possible to obtain an approximate value for the correlation length of the turbulence spectrum using the value of l_b. At least two species are required to apply this method, and if $\gamma_1 = \gamma_2$, the correlation length cannot be estimated.

3.1. Method 1

Voyager observations during the solar minimum conditions near the end of 1977 showed that different anomalous species peaked at different energies. The location of the maxima, or indeed any other prominent spectral feature, can be used to deduce the rigidity dependence of the diffusion coefficient, provided the spectral features occur at the same values of κ for each species. For $\kappa \propto (w/c)P^{\gamma}$ the location of the maxima in the nonrelativistic limit depends on atomic mass A as

$$E_{\max} \propto A^{-2\gamma/(\gamma+1)} \quad (12)$$

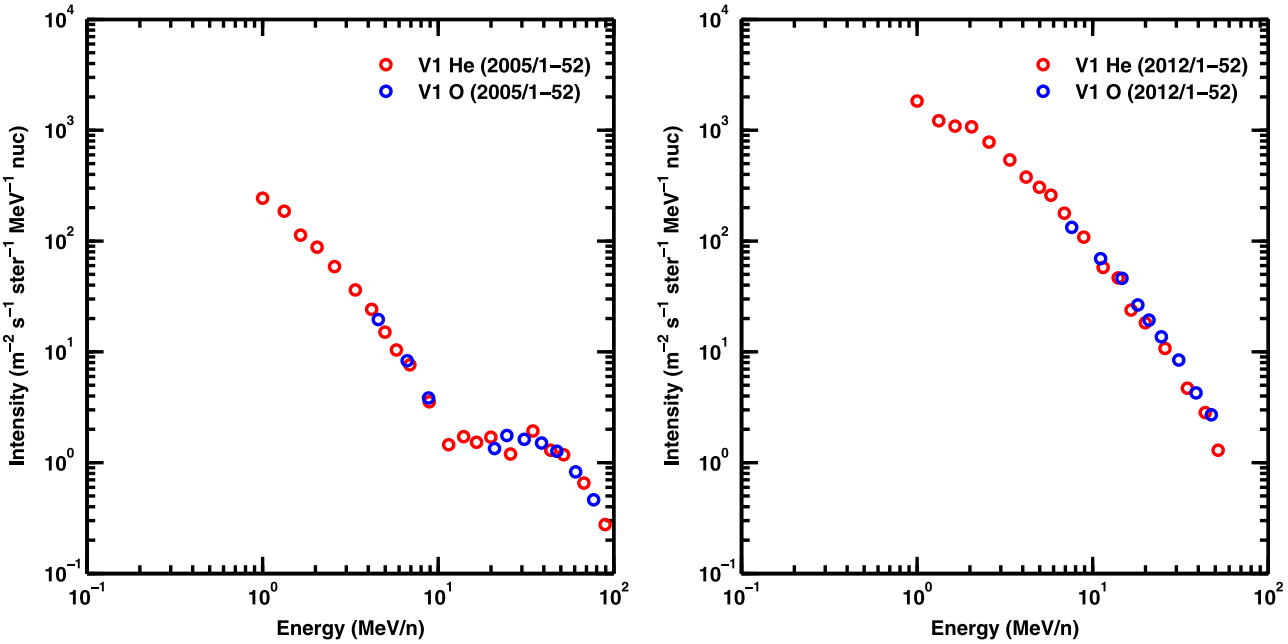

Figure 2. GCR corrected spectra of helium ions (red circles) and oxygen ions (blue circles) measured by *Voyager 1* at the TS (left panel) and in the heliosheath (right panel). In the left panel, the oxygen energy scaling factor and the intensity scaling factor are 3 and 1.95, respectively, up to 12 MeV n^{-1}and 5 and 1.66, respectively, for higher energies, whereas in the right panel they are equal to 5 and 1.71, respectively, for all energies.

(see Cummings et al. 1984; Cummings & Stone 2008). By using an appropriate energy scaling factor and an intensity scaling factor (to account for the differences in source strengths), it is possible to overlay the spectra of different species on top of each other and estimate the coefficient γ. Here we apply a similar method to the helium and oxygen ion data from *V1* to determine the rigidity dependence of the diffusion coefficient $\kappa_{\|}$.

Figure 2 shows the *V1* ACR spectrum from the time just after the TS crossing (early 2005, left panel), featuring a prominent hump at intermediate energies, and the evolved spectrum in early 2012 (right panel) for He (red circles) and O (blue circles) anomalous species. The spectra have been corrected for galactic cosmic rays (GCRs) based on the observed carbon energy spectrum, which lacks a significant anomalous component. The oxygen data points were scaled in energy (using Equation (12)) and intensity to match the helium data. By overlaying the spectra of helium and oxygen, we found the oxygen intensity and energy scaling factors that give the best fit (minimum χ^2 values). For the 2005 spectra, we found that the energy factor is about 3 ($\sim\gamma = 0.66$) between 1 and 12 MeV n^{-1} and it is about 5 ($\sim\gamma = 1.4$) at higher energies. The corresponding intensity factors are 1.95 and 1.66, respectively. Therefore, we adopted E_0 as 12 MeV n^{-1} for He and 4 MeV n^{-1} for O. The difference in energy and intensity scaling factors suggests that the anomalous spectrum may be separated into two components. The low-energy particle population (<12 MeV n^{-1} for He and < 4 MeV n^{-1} for O) may be referred to as the TS particles (TSPs; Stone et al. 2005, 2008; Cummings 2011), whereas the higher energies are the ACRs. For the spectra in 2012, the best-fit energy factor is about 5 ($\sim\gamma = 1.4$) at all energies. In this case, the oxygen intensities were multiplied by a factor of 1.71. As a result of the unrolling ACRs, here it is difficult to distinguish between TSPs and ACRs. Note that, in our simulations (see Section 4), we do not separate TSPs from ACRs as a different population.

3.2. Method 2

The main purpose of this method is to estimate the rigidity dependence (γ), such that if there is a change in γ, it occurs at the same rigidity (or gyroradius) for every particle species. As we discussed earlier, the break in the diffusion coefficient (or change in γ) occurs at a specific gyroradius r_g^* for all of the particle species. This r_g^* is close to l_b. Then, the correlation length (l_c) can be computed as $l_c = 0.79 l_b$ for the power spectrum given in le Roux et al. (1999).

Assuming $\kappa \propto (w/c)P^{\gamma}$ for He and O particles that have the same diffusion coefficient, one can obtain the value of γ as (see Appendix A1 for the derivation)

$$\gamma = \frac{\ln\left(A_{\rm O}/A_{\rm He}\right)}{\ln\left(P_{\rm O}/P_{\rm He}\right)} - 1, \tag{13}$$

where A_* and P_* are the atomic mass and the rigidity of oxygen and helium particles. Therefore it is possible to estimate γ using Equation (13) if the $\left(P_{\rm O}/P_{\rm He}\right)$ ratio is known. The next step is to use the He and O data from 2005 and 2012 to estimate this ratio.

In the top panels of Figure 3, the helium data were fit with a polynomial, and then a selected set of oxygen data points (eight points) were multiplied by intensity factors of 1.65 and 1.43 for data from 2005 (left panel) and 2012 (right panel), respectively, to match similar spectral features in the He spectrum. For each of the above oxygen data points, the corresponding helium rigidity that gives the same intensity was found. Then, the ratio $P_{\rm O}/P_{\rm He}$ was calculated as a function of $P_{\rm O}$, as shown by the solid lines in the bottom two panels. In the bottom left panel, this ratio is nearly constant up to around

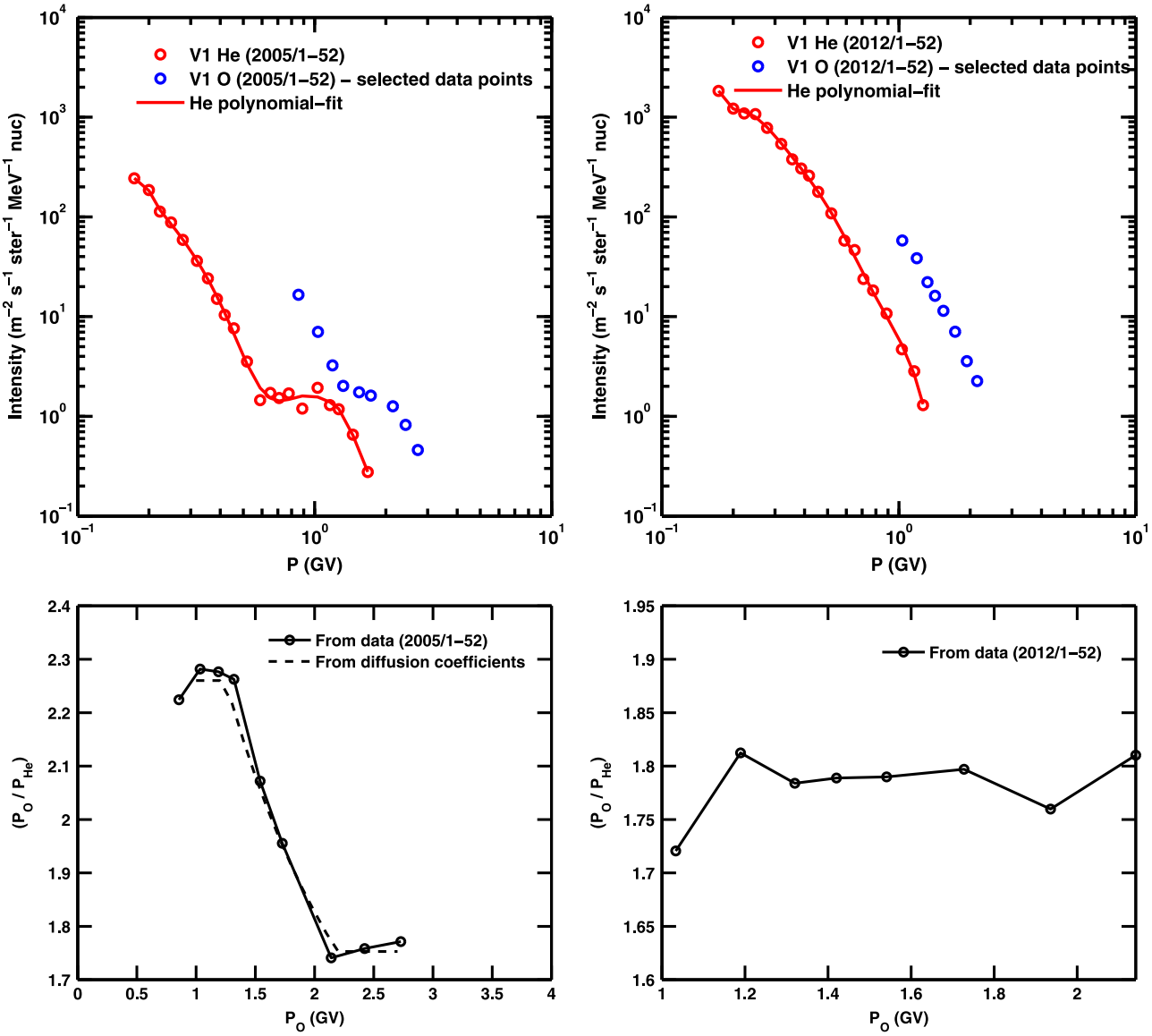

Figure 3. Top two panels show the He and O data aligned in intensity (to match spectral features) plotted as a function of rigidity at the TS (left panel) and in the heliosheath (right panel). Red lines show the polynomial fits to the He data. The bottom two panels show the rigidity ratio between O and He at the same (scaled) intensity as a function of the rigidity of O. The solid lines were calculated using *V1* data, and the dashed line (bottom left) was obtained from Equation (16) (see text).

~1.25 GV; then there is a gradient until ~2.1 GV, followed by another plateau. Estimating γ values for this case is not straightforward; this will be discussed in the next paragraph. In the right panel, the ratio is nearly constant with a mean of 1.78. Note that, in this case, we chose the intensity factor that gave the minimum standard error because there are no prominent spectral features here as in the left panel. Using this ratio in Equation (13) gives $\gamma = 1.4$, which is the same value we obtained for the data from 2012 in Method 1.

One can redefine Equations (10) and (11) as follows, assuming that the change in γ occurs at rigidity P_b for both He and O:

$$\kappa_{\parallel 3} = \begin{cases} \kappa_{03}\dfrac{w}{c}\left(\dfrac{P}{P_0}\right)^{\gamma_1}\dfrac{B^2}{\langle \delta B^2\rangle} & ; P \leqslant P_b \\ \kappa_{03}\dfrac{w}{c}\left(\dfrac{P_b}{P_0}\right)^{\gamma_1}\left(\dfrac{P}{P_b}\right)^{\gamma_2}\dfrac{B^2}{\langle \delta B^2\rangle} & ; P \geqslant P_b, \end{cases} \quad (14)$$

$$\kappa_{\perp 3} = a_2\kappa_{\parallel 3}\frac{\langle \delta B^2\rangle}{B^2}, \quad (15)$$

where κ_{03} is a constant. Next, the ratio P_O/P_{He} was calculated as a function of P_O using the following equations (see Appendix A.2 for the derivation):

$$\left(\frac{P_O}{P_{He}}\right) = \begin{cases} \left(\dfrac{A_O}{A_{He}}\right)^{1/(1+\gamma_1)} & ; P_O \leqslant P_b \\ \left[\left(\dfrac{A_O}{A_{He}}\right)\left(\dfrac{P_O}{P_b}\right)^{(\gamma_1-\gamma_2)}\right]^{1/(1+\gamma_1)} & ; P_b \leqslant P_O \leqslant P_t \\ \left(\dfrac{A_O}{A_{He}}\right)^{1/(1+\gamma_2)} & ; P_O \geqslant P_t, \end{cases} \quad (16)$$

where $P_t = P_b\left(\frac{A_O}{A_{He}}\right)^{1/(1+\gamma_2)}$.

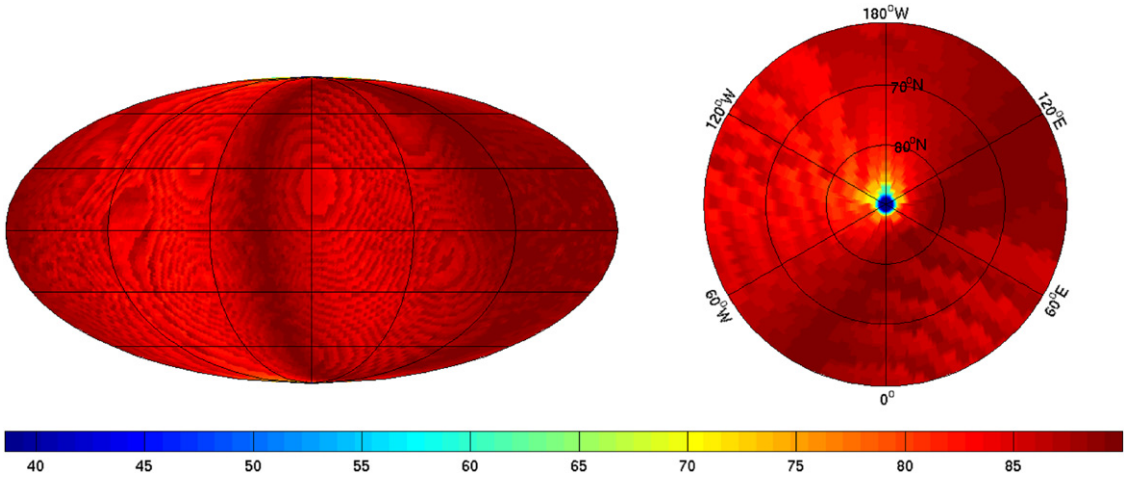

Figure 4. Left: color map of the shock normal angle θ_{BN} at the TS. The nose of the heliosphere is at the center of the map. Right: θ_{BN} viewed from above the north pole.

Next, the appropriate γ_1, γ_2, and P_b were chosen to match the solid line in the bottom left panel. We applied $\gamma_1 = 0.7$, $\gamma_2 = 1.47$, and $P_b = 1.25$ GV in Equation (16) to obtain the dashed line in the bottom left panel. In quasi-linear terms, the P^γ dependence in the diffusion coefficient entails a power-law turbulent spectrum $\sim k^{\gamma-2}$, where k is the wavenumber. Therefore, γ values of 0.7 and 1.47 yield the turbulence power-law slopes of −1.3 and −0.53, respectively. According to this method, the break in the diffusion coefficient (P_b) occurs at 1.25 GV, which corresponds to $l_c = 0.2$ AU with a 1.05 μG magnetic field just behind the TS, according to our plasma background. The change in γ to 1.4 for all energies in 2012 could be related to a decrease in the turbulence correlation length during this time period. Therefore, this method predicts a larger correlation length in 2005 (moderate solar activity) than in 2012 (low solar activity), as discussed above.

Generally, the two methods produce similar power-law slopes. The first method gives clues for the existence of two separate ACR populations at the TS, whereas the second method suggests that the spectral shape may have changed from 2005 to 2012 as a result of a decrease in the turbulent correlation length.

4. SIMULATED RESULTS AND *V1* OBSERVATIONS

The spectra of He^+ and O^+ ions were computed using the numerical transport code for the two diffusion models described by Equations (4), (5) and (6), (7), respectively. The diffusion coefficient's free parameters were chosen such as to provide the best agreement with *V1* observations at the TS and in the heliosheath. Two sets of simulations were performed, one for moderate solar maximum conditions (HCS tile angle of 55°) and the other for the solar minimum with a flat HCS. The first and second diffusion models are based on the method described in Section 3.1, and the third model is based on Section 3.2. Therefore, in models 1 and 2, the diffusion coefficients were calculated with $\gamma_1 = 0.66$ and $\gamma_2 = 1.4$, with the break between the two at 12 MeV n^{-1} for helium and 4 MeV n^{-1} for oxygen for the first set of simulations. For the second set we used $\gamma = 1.4$ at all energies. In diffusion model 3, γ_1 and γ_2 were set to 0.7 and 1.47, respectively, with the break at 1.25 GV (50.7 MeV n^{-1} for helium and 3.25 MeV n^{-1} for oxygen) for the first set. The second set of simulations in model 3 is equivalent to the ones in model 2 ($\gamma = 1.4$). Therefore, no simulations were run for the second set in diffusion model 3.

4.1. Diffusion Model 1

This model is based on Equations (8) and (9). The list of relevant parameters is provided in Table 1. The values of κ_{01} were chosen based on the criterion that the diffusion coefficients are the same at the minimum energy (0.5 MeV n^{-1}) in both simulations.

We were unable to achieve a good match between the data and simulation results, especially at higher energies, for this diffusion model and a uniform source along the shock. However, the strength of the source (i.e., the rate of injection into the DSA) is unlikely to be the same everywhere along the TS. It is often assumed that the pickup ion (PUI) injection efficiency is higher in the regions where the angle between the magnetic field and the shock normal, θ_{BN}, is small (Zank et al. 2006). To see whether this is of relevance to the TS, which after all is a nearly perpendicular shock (Burlaga et al. 2009), we calculated θ_{BN} using the model background plasma velocity to compute the shock normal vector similar to Abraham-Shrauner (1972) and Li et al. (2008). Figure 4 shows the calculated θ_{BN} as a "Mollweide" projection in the left panel and the region near the north pole in the right panel (a "stereographic" projection). It is evident that $\theta_{BN} = 80°-90°$ everywhere except very close to the poles, where it drops to 40°. These results are in contrast with Scherer & Fahr (2009), who argued that the shock normal angle can be as low as 65° on the flanks of the TS.

At first glance the above result might suggest that ACRs are born only near the poles. However, Schwadron et al. (1999) suggested that PUIs are enhanced at high-latitude compression regions. Also, according to Schwadron & McComas (2003), the mixing of fast and slow solar wind produces shear regions where the solar magnetic field is radial at latitudes close to *V1*, and in those regions PUI injection would be much more efficient. However, Giacalone et al. (1994) and Zank (1999) have shown that, even at a perpendicular shock, PUIs can be accelerated to sufficiently high energies. Further, at the *V2* TS crossing, a large increase in the intensity of ~40 keV ions was observed (Decker et al. 2008), and Giacalone & Decker (2010)

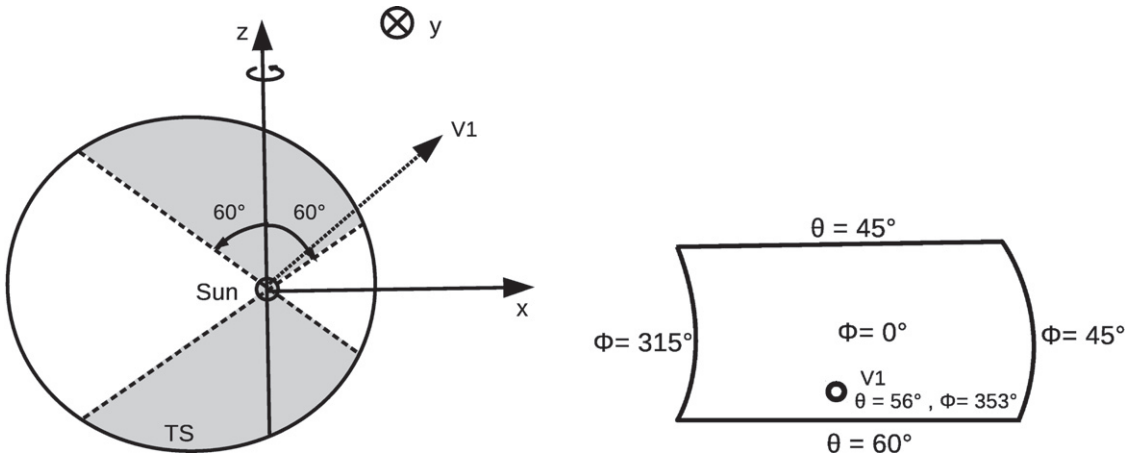

Figure 5. Left: the PUI injection region used in the first scenario (shaded), "polar injection." Right: the injection region in the second scenario, "nose injection." See text for further details. The direction toward *V1* is identified in each panel.

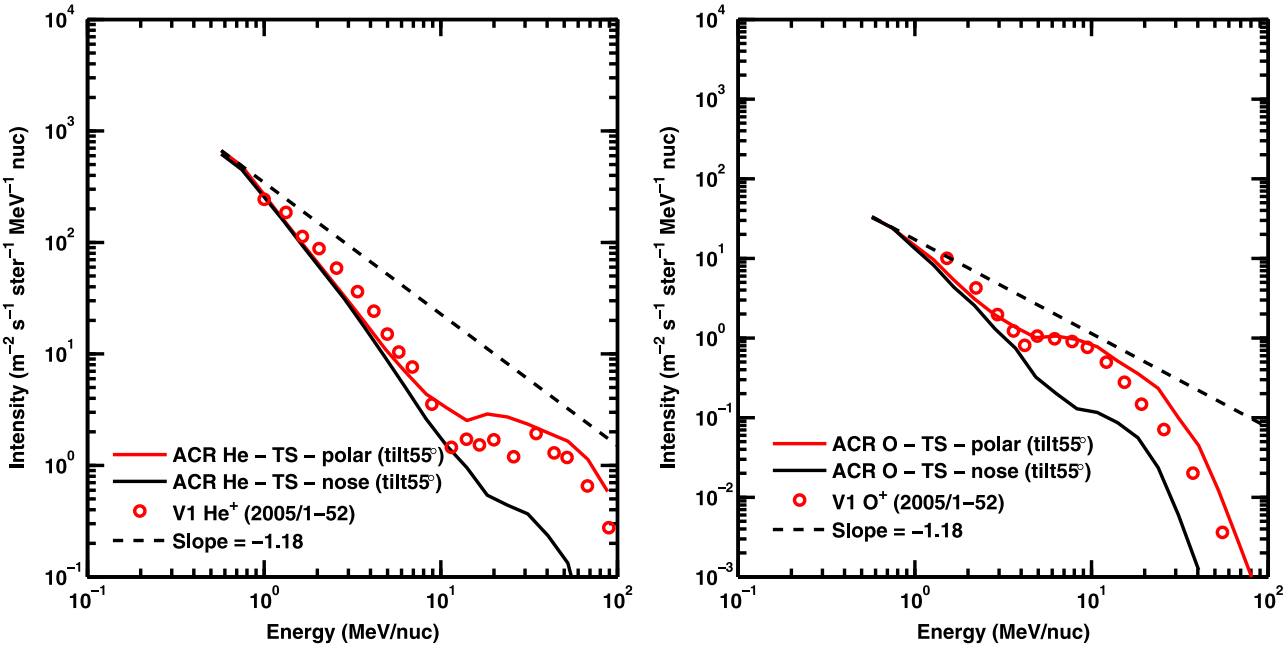

Figure 6. Left: ACR helium spectra at the TS (near solar maximum) using diffusion model 1. Spectra shown with red (black) lines were obtained with the polar (nose) injection scenario. *V1* observations during this time period are shown with red circles. The dashed line is the power law for a shock with a compression ratio of 3.2. Right: same for ACR oxygen.

argued that a combination of shock drift and field line meandering could accelerate PUIs to hundreds of kiloelectronvolts.

Because it was difficult to obtain even a qualitative fit to the observations by limiting injection to a few degrees from the poles, we used a wider region extending down to 60° from the polar axis, as shown by the shaded region in the left panel of Figure 5. It is essential that the *V1* direction (56°) lies inside the shaded area, or the lower energy part of the spectrum could not be reproduced. We have also investigated a second scenario where injection occurred only inside the rectangular region shown in the right panel of Figure 5. From here onward, we will call the injection regions in the left and right panels as the "polar injection" and the "nose injection," respectively.

We now turn to the simulation results. Figure 6 shows differential intensities of the two ACR species as a function of kinetic energy per nucleon from the model and *V1* observations. Here the red lines show the simulated spectra at the TS near solar maximum conditions along the *V1* direction for He (left panel) and O (right panel), obtained with the first source scenario. The red circles are from *V1* data recorded in early 2005, soon after its crossing of the TS. The dashed line is the "expected" power law for a shock with a compression ratio of 3.2. The actual spectra (red lines) consist of a power-law-like region up to the break point energy E_0 (see Section 2; 12 MeV n^{-1} for He and 4 MeV n^{-1} for O), followed by a "hump" and a gradual rollover beyond that. The black lines show the spectra from the simulation with injection limited to the region shown in the right panel of Figure 5. Note that the injection region in the right panel is a subset of the left panel. The red lines overlap with the black lines at lower energies (up to 5 MeV n^{-1} for helium and 2 MeV n^{-1} for oxygen). Therefore, the low-energy anomalous spectrum can be reproduced by limiting the injection to the region near the *V1*

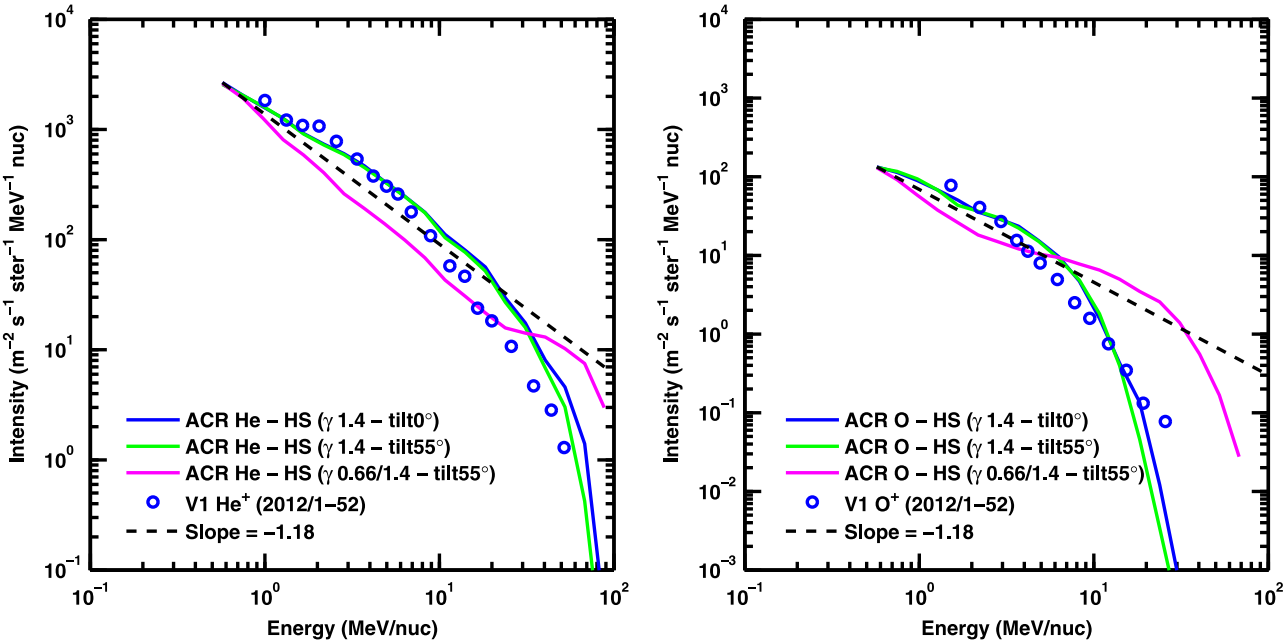

Figure 7. Simulated spectra in the heliosheath using diffusion model 1, with injection restricted to high latitudes, of anomalous helium (left panel) and oxygen (right panel), compared with the spectra observed by *V1* in early 2012 (blue circles). The blue lines are spectra obtained for a flat current sheet and $\gamma = 1.4$, the green lines are for a warped HCS (55°) and $\gamma = 1.4$, and the magenta lines are for a warped HCS (55°) and the same γ as in the solar maximum case.

location. This is consistent with the idea of TSPs that are believed to be accelerated at the TS near the spacecraft. The first source model gives a better agreement with both the TSP and ACR parts (as described in Section 3.1) of the observed spectrum compared to the second source model.

Figure 7 shows the simulated spectra of anomalous helium (left panel) and oxygen (right panel) in the heliosheath (TS + 30 AU) during solar minimum conditions, using source model 1. This is compared with the "unrolled" ACR spectra observed by *V1* at the beginning of 2012. For this period, the injection rate was enhanced by a factor of 4 compared to the simulation shown in Figure 6, which was required to fit the *V1* spectra in the heliosheath. The blue lines show the spectra using a flat current sheet with $\gamma = 1.4$, whereas the green colored lines show the spectra for the HCS tilt of 55° with $\gamma = 1.4$. The two are quite similar, which implies that drifts have a weaker influence on the unfolding spectra at the *V1* latitude. The cutoffs occur at ~25 MeV n^{-1} for helium and ~7.5 MeV n^{-1} for oxygen ions.

Also shown in Figure 7 are simulations using moderate solar maximum conditions (similar to Figure 6) as the magenta lines. These spectra do not agree with the observations at all. However, the agreement with the solar minimum simulations is reasonable for helium, although the measured oxygen spectrum is still harder than the simulated spectrum.

4.2. Diffusion Model 2

The second diffusion model is based on Equations (10) and (11), and the list of relevant parameters is again given in Table 1. Note that κ_{02} is much larger than κ_{01}. This is because in the first diffusion model the parallel diffusion coefficient is inversely proportional to the magnetic field, whereas in the second model it is proportional to the square of the field. Note that for this model a uniform source was assumed along the shock, in contrast to the previous subsection.

Figure 8 shows the simulated spectra at the TS under a high solar activity condition for He (left panel) and O (right panel) ions using the second diffusion model. Compared with the first model (Figure 6), the higher energy part of the anomalous helium spectrum (>10 MeV n^{-1}) agrees better with the observational data. The oxygen TS spectrum appears to be very similar to that obtained with diffusion model 1.

Figure 9 plots the spectra calculated for the heliosheath using the second diffusion model. In this case the intensities were multiplied by a factor of 8 to match the data. The meaning of the different color lines is the same as in Figure 7. Again, we see that blue and green lines give a better agreement with the observations than do the magenta lines. In contrast to model 1, this model produces no hump in the spectra. Instead, there is a long power-law-like region followed by an exponential rollover. In general, the diffusion model 2 spectra in the heliosheath agree better with the *V1* observation data than do the diffusion model 1 spectra.

4.3. Diffusion Model 3

For the third diffusion model, Equations (14) and (15) were applied (see Table 1 for the relevant parameters used). Figure 10 shows the simulated spectra at the TS using this model for He (left panel) and O (right panel). In comparison with Figure 8, the anomalous He spectrum does not show the same rollover after ~10 MeV n^{-1} in this case, whereas the O spectrum appears to be similar. In diffusion model 2 the diffusion dependence on rigidity becomes steeper after 12 MeV n^{-1} for helium ($\gamma = 0.66$ to $\gamma = 1.4$), whereas in model 3 $\gamma = 0.7$ up to 50.7 MeV n^{-1}. As a result, one would not expect the dip to occur at the same energy in the two models. For oxygen, the break energy and the γ values are similar in both models 2 and 3. Therefore, the oxygen spectra near the TS are nearly identical in Figures 8 and 10. The heliosheath spectra in this model would produce exactly the same

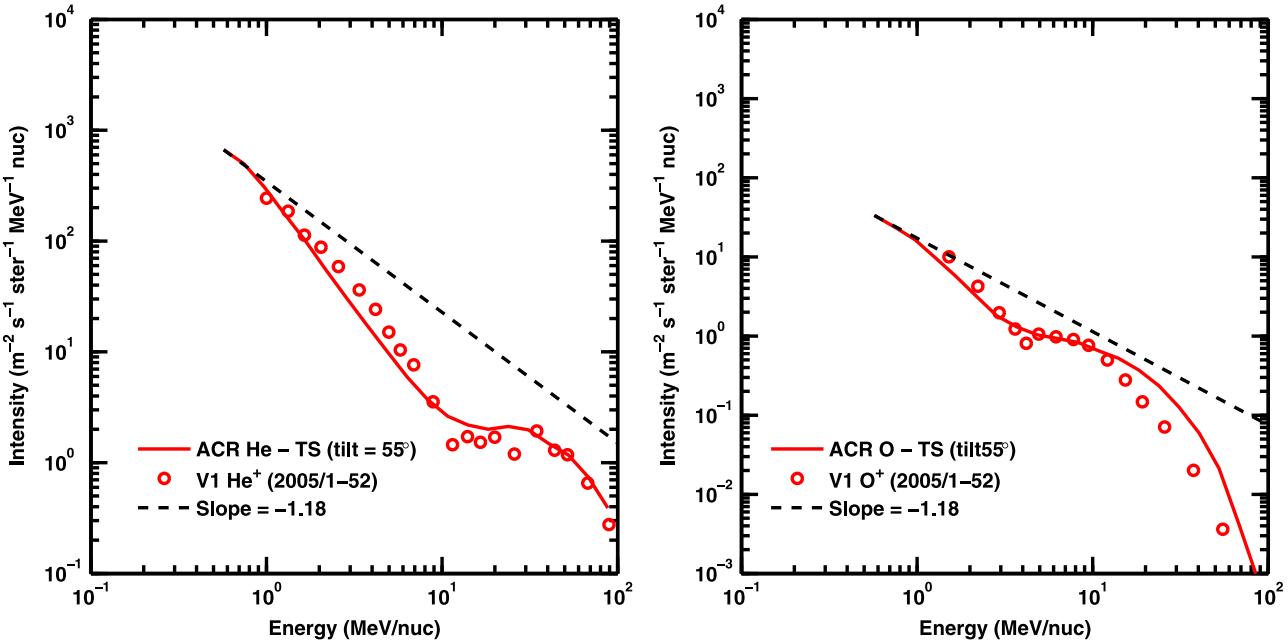

Figure 8. Simulated energy spectra (red lines) using diffusion model 2 and a uniform source at the TS for helium (left panel) and oxygen (right panel) ions, plotted alongside *V1* observations (red circles).

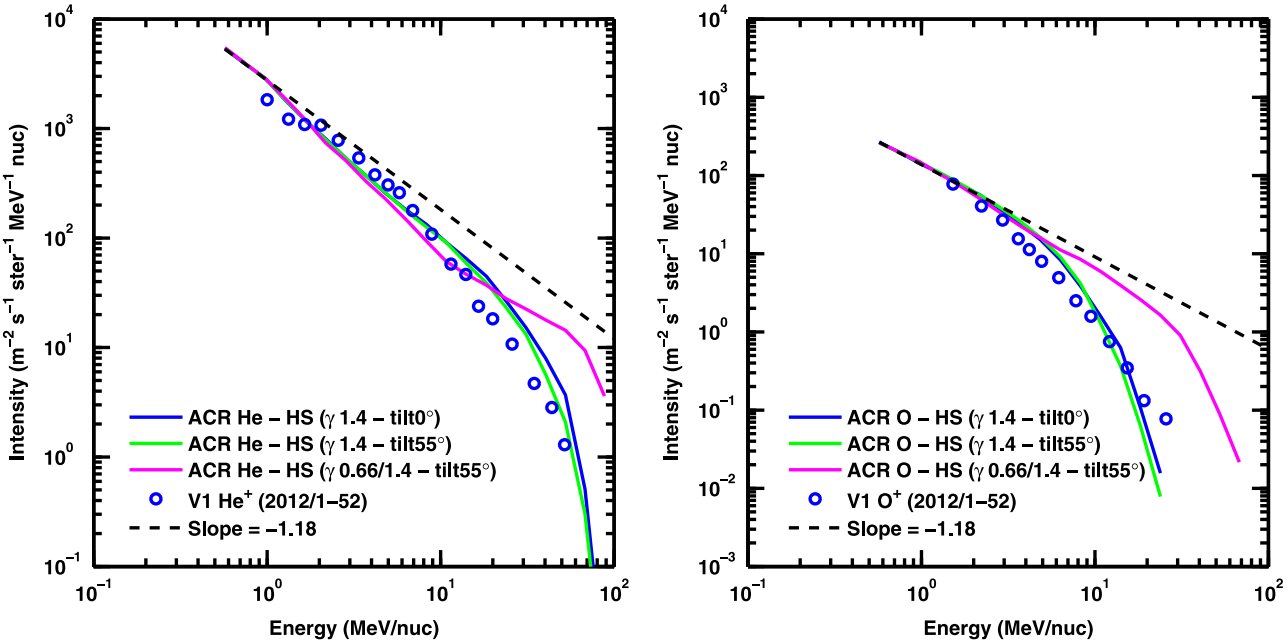

Figure 9. Same as Figure 7, but for diffusion model 2 with a uniform source.

spectra as in Figure 9. Therefore, no simulations are needed for this case.

The simulated spectra were compared with the observations quantitatively by calculating χ^2 values (see Table 1). Overall, diffusion model 2 shows better agreement (smallest χ^2) with the observations compared with the other two models. In conclusion, we were able to obtain a reasonable fit to the *V1* helium spectra both at the TS and in the heliosheath using all three diffusion models. However, we were unable to obtain a good fit at high energies (>20 MeV n^{-1}) for oxygen using the same parameters. One possible cause of this disagreement is that higher energy oxygen ions have a significant multiply charged component (Jokipii 1996; Mewaldt et al. 1996) that was not included in our model (see Section 5). Furthermore, the larger population of GCRs present at these energies may have an effect on the spectra, although our data were corrected for GCRs. It also appears that drifts do not contribute significantly to the process of "unfolding" of the spectra in the heliosheath.

4.4. Radial Intensity Profiles

To help understand the spatial variation of low-energy ACRs in the heliosheath, we computed intensities of 5 MeV n^{-1} helium ions as a function of radial distance. The second

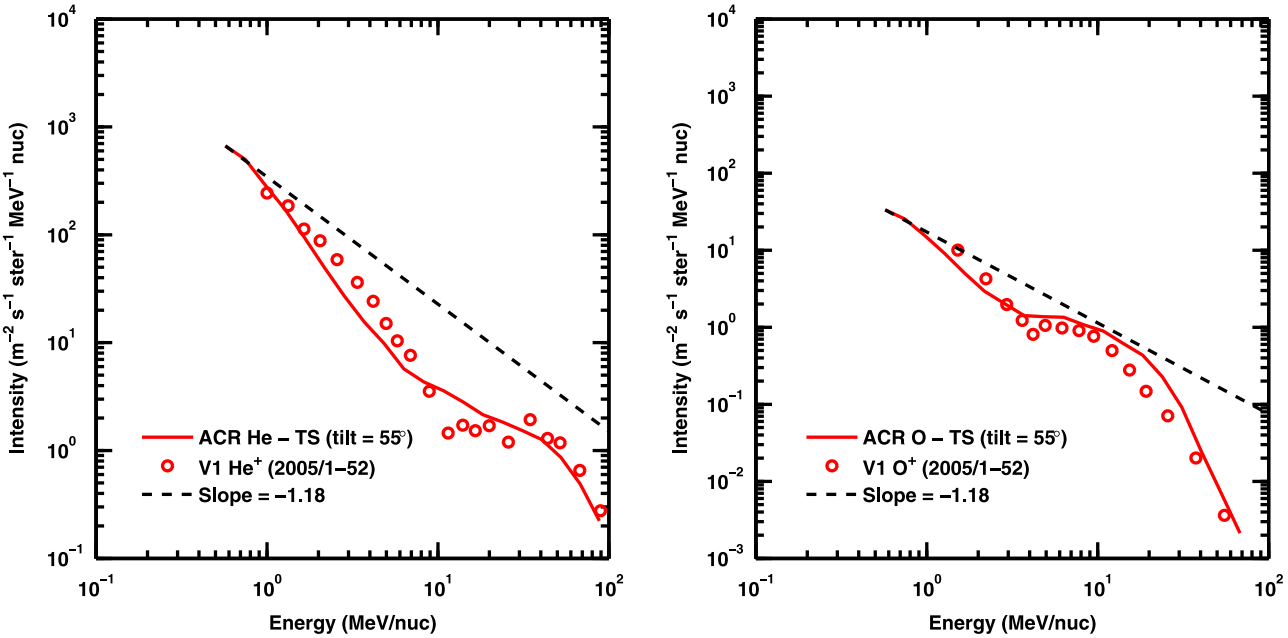

Figure 10. Same as Figure 8, but for diffusion model 3 with a uniform source.

diffusion model was used, which was in a better agreement with observations in the heliosheath. Our simulation results were compared with 4.6–5.4 MeV n^{-1} *V1* ACR He data from early 2004 to the end of 2012.

A time-independent heliospheric background was used to model time-dependent solar cycle variations. In our simulations, about six months is needed for ACRs to reach the energy of 5 MeV n^{-1} starting from 0.5 MeV n^{-1} (Senanayake & Florinski 2013). Therefore, one could assume that during a trajectory lifetime, the solar conditions do not change. We used fixed diffusion coefficients and source intensities corresponding to the trajectory end points (i.e., detection points). For simplicity, the HCS tilt angle was maintained at 55° regardless of the phase of the solar cycle. This is a reasonable assumption because, as our earlier results suggest, drift effects are not significant at the latitude of *V1*. Here, three cases were considered. First, we used a fixed diffusion coefficient and source intensity. In the second set of simulations, we varied both the diffusion and the source strength depending on the trajectory end points (see below for details). In the third case we fixed the diffusion and varied only the source strength to determine which is more important for low-energy ACRs.

In the first method, we used the "solar maximum" rigidity dependence of the diffusion coefficient with $E_0 = 12$ MeV n^{-1} and a constant source intensity. The second method was an attempt to incorporate solar cycle variations in the diffusive mean free paths and source intensities into a model that is based on a steady-state background. To model ACR intensities between the TS and the HP measured by *V1* (that were recorded during the period when the solar-wind conditions were changing from moderate solar maximum conditions to a solar minimum), we performed a series of 30 simulations, each with a diffusion coefficient fixed at the solar cycle phase corresponding to the end of the trajectory. For the end points inside the TS, solar maximum conditions were used, and for those beyond 120 AU, solar minimum conditions were applied. For the end points lying in between ($90 < r < 120$ AU), we assumed that the TS source intensity increased linearly, from 1.0 for the detector at 90 AU to 6.0 for the detector at 120 AU seven years later. The value of E_0 was set to 12 MeV n^{-1} at 90 AU and decreased linearly to 0.5 MeV n^{-1} at 120 AU. In the third method we varied only the source intensities, with $E_0 = 12$ MeV n^{-1} for all trajectories.

The results of this comparison are shown in Figure 11. In the data (left panel), intensities were steadily increasing after the TS crossing, up to about 110 AU. They remained steady between 110 and 120 AU, followed by a rapid drop at the heliocliff. As mentioned in Section 2, the distance to the HP in the MHD model (160 AU) greatly exceeds the actual distance (122 AU in 2012). Most of the current MHD models predict an HP standoff distance of about 140–150 AU (Pogorelov et al. 2004; Opher et al. 2006; Borovikov et al. 2011). In our model this distance is about 10–20 AU larger compared to the above models because of a relatively fast plasma velocity that was used at the inner boundary. On the other hand, the TS in the *V1* direction was at 90 AU, which is close to the actual shock crossing distance. As mentioned in Section 2, *V1* crossed the TS during near solar maximum conditions in the inner heliosphere. Consequently, one would expect a larger distance to the HP at this time because of the high dynamic pressure of the solar wind. *V1* crossed the HP during an unusually weak solar cycle, and it is likely that the actual HP was so much closer to the Sun than in the simulations because of the low dynamic pressure of the solar wind.

In the right panel of Figure 11, green, black, and magenta lines show the simulated intensities of 5 MeV/n anomalous helium along the *V1* trajectory for the three scenarios described previously. The steady-state simulation (green line) shows an increase in intensity between 90 and 120 AU by a factor of ~3. Much of this enhancement is from arrival of the particles accelerated at the tailward part of the shock (McComas & Schwadron 2006; Kóta & Jokipii 2008; Guo et al. 2010; Kóta 2010; Senanayake & Florinski 2013). The increase is quite modest compared with the measured increase during this time period. When combined with solar cycle effects, including a source increase and the changes in the rigidity dependence of

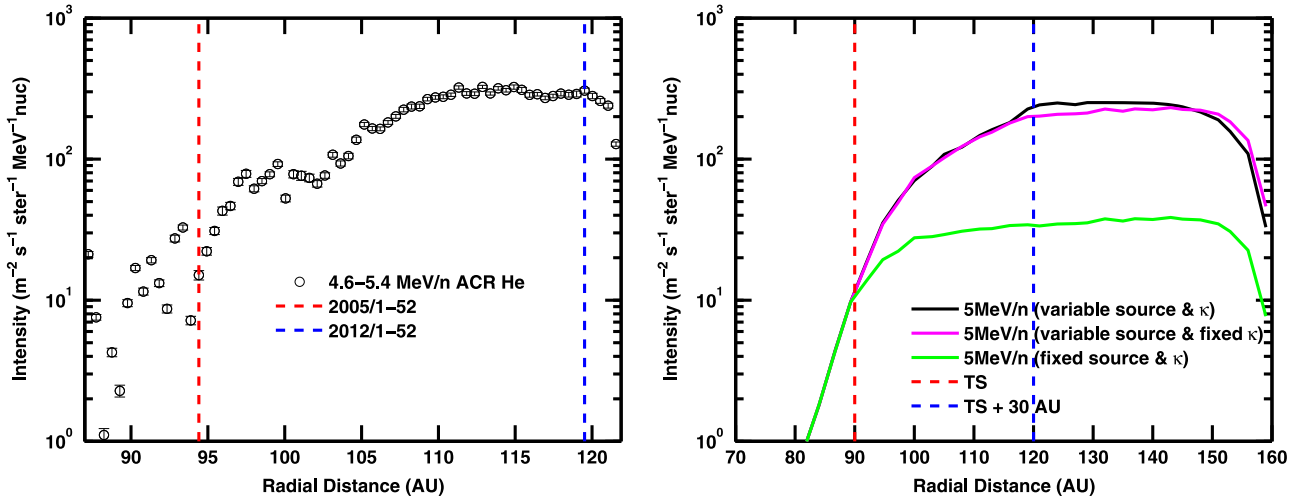

Figure 11. Radial profiles of 4.6–5.4 MeV n^{-1} He^{+} ions measured by *V1* (left panel) and the simulated 5 MeV n^{-1} anomalous He intensity (right panel). In the right panel, lines colored black, magenta, and green show the results obtained with variable injection and diffusion, variable injection and fixed diffusion, and fixed injection and diffusion, respectively (see text for details). The vertical dashed lines mark the locations where the spectra were plotted earlier (for example, in Figures 6 and 7 spectra are plotted at positions given by red and blue dashed lines, respectively).

the diffusion coefficients (black line), a factor of ∼20 increase is seen between the same distances, similar to the observation shown in the left panel. The magenta line shows the results obtained by only including a source increase. The black and magenta lines essentially coincide up to 115 AU, which suggests that up to this point diffusion changes do not have much impact on 5 MeV n^{-1} particles. Afterward, as a result of the increase in diffusion (E_0 becoming less than 5 MeV n^{-1}), from 115 to 145 AU, the black line overshoots the magenta line. However, on approach to the HP, the black line intensity starts to decrease earlier compared to the magenta line. This is a result of faster diffusion for the case shown in the black line compared to the magenta line. Because of larger diffusion, ions reach the LISM faster, producing an earlier drop in intensity.

Note that *V1* intensities remained almost unchanged from 110 AU (mid-2010) until the crossing of the HP at 122 AU. Indeed, there was little change in solar activity during this period, because the minimum between cycles 23 and 24 lasted much longer compared with the previous solar cycles (Jian et al. 2011; Russell et al. 2013). This is reproduced in our simulations by using solar-minimum-like conditions for trajectory end points lying beyond 120 AU. Because the HP is located much farther away in the simulations, the results should not be directly compared with the observations at such large distances. However, our simulation results do provide important insights into the ACR behavior in the heliosheath. It is evident that lower energy anomalous ions became enhanced in the heliosheath mainly because of an increase in the source intensity between 2005 and 2012.

5. DISCUSSION

The *Voyager* observations of ACRs at the TS were puzzling, and the shape of the spectra could not be explained by steady DSA. The observed spectra consisted of a power-law-like region at low energies with a dip at intermediate energies. Lower energy intensities started to increase as the spacecraft traveled deeper into the heliosheath, and eventually the intermediate-energy part of the spectrum recovered. To explain this recovery, we adapted our earlier model (Senanayake & Florinski 2013) where ACR acceleration occurred primarily in the tail region of the TS, and we varied the transport coefficients and the source intensities to model the solar cycle effects. Two types of simulations were performed. In the first scenario, moderate solar maximum conditions were used to model *V1* spectra at the TS in early 2005. The second scenario used solar minimum conditions in an attempt to reproduce *V1* data from early 2012. For the solar maximum case, a warped HCS with a tilt of 55° was used; a flat HCS was used during the solar minimum. The rigidity dependence of the diffusion coefficient was estimated by comparing He and O spectra from *V1* in 2005 and 2012 using two different methods. In method 1 (Section 3.1), the characteristic spectral features of different species are overlaid to estimate the γ values, whereas in method 2 (Section 3.2), γ was estimated by comparing the rigidity ratio of oxygen to helium (P_O/P_{He}). Both methods showed similar spectral slopes during the two periods.

We developed three different diffusion models to explain *V1* observations at the TS and in the heliosheath. We also investigated the effect of varying the source region on the spectra along the *V1* trajectory. The helium spectra obtained with either model agree reasonably well with the spectra measured at the TS and near the HP using the diffusion coefficients appropriate for the phase of the solar cycle when the measurements were done. Our simulations of the radial profile of 5 MeV n^{-1} helium reproduced a large (factor of 20) gradual enhancement measured during the *V1* journey through the heliosheath. Although we do not discuss *V2* observations here, they could be modeled using the same approach.

The inclusion of solar cycle effects was done in a simplified fashion, by "freezing" the turbulence conditions at the end of the particle's trajectory (i.e., at the time the observation was performed). A more accurate (and a much more complicated) approach could use a fully time-dependent plasma background of the heliosphere over a solar cycle. Nonetheless, our simpler models give important clues to understanding the spectral changes of anomalous ions along the *V1* trajectory.

We also found that it was difficult to reconcile simulated anomalous oxygen spectra with the observations, especially at higher energies (>20 MeV n^{-1}). The high-energy oxygen ions contain a higher percentage of GCRs. Although our data were

corrected for GCRs, there could be some uncertainties. Moreover, high-energy oxygen ACRs contain a significant fraction of multiply charged O ions (Jokipii 1996; Mewaldt et al. 1996), which may affect the oxygen spectra. A better match could have been obtained for anomalous oxygen if multiply charged O ACRs were taken into account. This will be investigated in our future work.

The steeper rigidity dependence of the diffusion coefficient at low-energy ACRs (<12 MeV n^{-1} for He and <4 MeV n^{-1} for O) in 2012 can be described in two ways. The first is to assume that ACRs and TSPs are two separate populations (see Section 3.1). Then, if one assumes that the TSP spectrum did not vary much over time (Stone et al. 2008), the rigidity dependence in the TSP region became steeper as a result of unfolding ACRs, producing a harder spectrum at low energies. According to our simulations (Figure 6), it appears that low-energy ACRs (or TSPs) are injected and accelerated close to the spacecraft location. However, we do not distinguish TSPs and ACRs as two different populations in this work. The other approach is to assume that the entire spectrum is a single population (see Section 3.2). This requires, as discussed in Section 2, that the turbulence correlation length would have decreased from 2005 to 2012, resulting in a steeper rigidity dependence for the latter period. Nevertheless, at much lower energies (e.g., 5 MeV n^{-1} for He), it is likely that the intensity increase (a factor of ~20) was a combination of a source strength increase (a factor of ~7) and also particles coming from the tail (a factor of ~3).

In Section 3.2, we were able to estimate the correlation length during the moderate solar maximum conditions in early 2005 at the TS. Our method yields the value of about 0.2 AU during this period. The turbulence model of Isenberg et al. (2010) suggests that the correlation length is about 0.2 AU near the TS. Other models predict it to be within the range (0.05–0.15) AU near the TS (Breech et al. 2008; Usmanov et al. 2011; Adhikari et al. 2014). Note that in our simulations we assumed that correlation length remains the same during a particle trajectory. In reality, it changes with time as well as the distance from the Sun.

Because of the higher global solar-wind flux in solar maximum, the PUI flux is expected to be higher than the flux in solar minimum (e.g., Rucinski et al. 2003). Then, one would expect more ACR source particles in solar maximum compared to minimum. However, from 2005 (moderate maximum) to 2012 (minimum), lower energy ACR He^+ (~1.0 MeV n^{-1}) and O^+ intensities (~1.5 MeV n^{-1}) have increased by a factor of ~8. It is out of scope of this model to explain these observations because we do not study the injection problem here. Nevertheless, it is likely that the transport and acceleration of these low-energy ions were much more efficient during solar minimum conditions compared to maximum conditions. In order to fit the observations, intensities had to be multiplied by an appropriate factor (see Table 1). However, the intensity of high-energy He^+ (>50 MeV n^{-1}) does not vary appreciably during this period (see the data points in the left panels of Figures 6 and 7). This would imply that the acceleration timescales are much longer for these energies compared to the source strength variation timescales from solar maximum to minimum. As a result of longer acceleration times, solar cycle variations are smoothed out at the highest energies. Further, our simulation results suggest that diffusion coefficients were larger during 2012 compared to 2005 at *V1*. This agrees with Cummings & Stone (2001, 2003) and Hill et al. (2002), who showed that the scattering mean free path is much larger during the solar minimum than during the solar maximum.

In summary, the spectral recovery of ACRs in the heliosheath at *V1* can be explained through a combination of intermediate-energy particles arriving from the tail of the TS (McComas & Schwadron 2006; Kóta & Jokipii 2008; Guo et al. 2010; Kóta 2010; Senanayake & Florinski 2013), an increase in the source strength, and a decrease in the turbulence correlation length resulting in longer diffusive mean free paths as the solar activity declined from 2005 to 2012. However, it is important to note that the enhancement in low-energy ions is almost entirely due to an increase in the source strength. Gradient and curvature drifts do not appear to have a profound effect on the spectral evolution at *V1*.

This work was supported in part by NASA grants NNX10AE46G, NNX11AO64G, NNX12AH44G, and NNX13AF99G and by NSF grant AGS-0955700.

APPENDIX
ANALYTIC EXPRESSIONS IN SECTION 3.2

A.1 Derivation of Equation (13)

Let us assume a diffusion coefficient of the form $\kappa \propto (w/c)P^{\gamma}$, where w is the particle speed and P is the rigidity. For the diffusion coefficients to be equal for He and O, we must have

$$\left(\frac{w_{\rm O}}{w_{\rm He}}\right)\left(\frac{P_{\rm O}}{P_{\rm He}}\right)^{\gamma} = 1. \tag{A1}$$

For singly charged ions $w = {\rm Pe}/({\rm Amc})$. Therefore, Equation (A1) can be rewritten as

$$\left(\frac{A_{\rm He}}{A_{\rm O}}\right)\left(\frac{P_{\rm O}}{P_{\rm He}}\right)^{\gamma+1} = 1, \tag{A2}$$

$$\gamma = \frac{\ln\left(A_{\rm O}/A_{\rm He}\right)}{\ln\left(P_{\rm O}/P_{\rm He}\right)} - 1. \tag{A3}$$

A.2 Derivation of Equation (16)

Assume that the rigidity dependence changes from γ_1 to γ_2 at rigidity P_b for both He and O. From Equation (14) it follows that

$$\kappa_{\parallel 3,{\rm He}} = \begin{cases} \kappa_{03}\dfrac{w}{c}\left(\dfrac{P_{\rm He}}{P_0}\right)^{\gamma_1}\dfrac{B^2}{\langle \delta B^2\rangle} & ; P_{\rm He} \leqslant P_b \\ \kappa_{03}\dfrac{w}{c}\left(\dfrac{P_b}{P_0}\right)^{\gamma_1}\left(\dfrac{P_{\rm He}}{P_b}\right)^{\gamma_2}\dfrac{B^2}{\langle \delta B^2\rangle} & ; P_{\rm He} \geqslant P_b, \end{cases} \tag{A4}$$

$$\kappa_{\parallel 3,{\rm O}} = \begin{cases} \kappa_{03}\dfrac{w}{c}\left(\dfrac{P_{\rm O}}{P_0}\right)^{\gamma_1}\dfrac{B^2}{\langle \delta B^2\rangle} & ; P_{\rm O} \leqslant P_b \\ \kappa_{03}\dfrac{w}{c}\left(\dfrac{P_b}{P_0}\right)^{\gamma_1}\left(\dfrac{P_{\rm O}}{P_b}\right)^{\gamma_2}\dfrac{B^2}{\langle \delta B^2\rangle} & ; P_{\rm O} \geqslant P_b. \end{cases} \tag{A5}$$

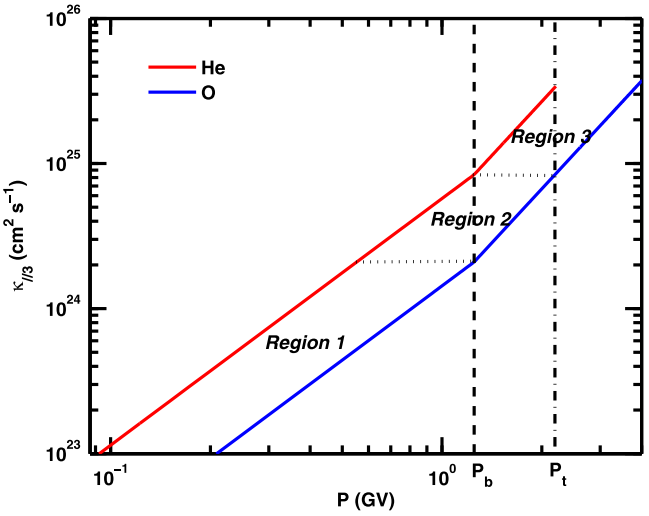

Figure 12. Diffusion coefficient just behind the TS along the *V1* direction, as a function of rigidity for He (red) and O (blue) using Equations (A4) and (A5). The dashed line and the dot-dashed lines mark the rigidity values P_b and P_t, respectively. The dotted lines separate three rigidity regions: region 1, $P_O \leqslant P_b$; region 2, $P_b \leqslant P_O \leqslant P_t$; and region 3, $P_O \geqslant P_t$.

Figure 12 shows the plot of diffusion coefficients as a function of rigidity for He (red line) and O (blue line). They were calculated just behind the TS, along the *V1* direction using the plasma background. The change in γ occurs at rigidity P_b for both He and O. Now compare rigidity ranges of He and O where the diffusion coefficients are the same using Equations (A4) and (A5), and then our goal is to obtain the rigidity ratio between O and He as a function of the rigidity of O. As shown in Figure 12, there are three regions that should be investigated. In region 1, both species have the same slope, so the rigidity ratio is a constant. However, in region 2, O has a steeper slope than does He; as a result, the rigidity ratio is a function of P_O. At P_t, the rigidity slopes of the species become the same again. Hence, again the rigidity ratio is a constant in region 3.

For the region $P_O \leqslant P_b$

$$\kappa_{03}\frac{w}{c}\left(\frac{P_{He}}{P_0}\right)^{\gamma_1}\frac{B^2}{\langle\delta B^2\rangle} = \kappa_{03}\frac{w}{c}\left(\frac{P_O}{P_0}\right)^{\gamma_1}\frac{B^2}{\langle\delta B^2\rangle}, \quad \text{(A6)}$$

$$\left(\frac{P_O}{P_{He}}\right) = \left(\frac{A_O}{A_{He}}\right)^{1/(1+\gamma_1)}. \quad \text{(A7)}$$

Then, for the region $P_b \leqslant P_O \leqslant P_t$

$$\kappa_{03}\frac{w}{c}\left(\frac{P_{He}}{P_0}\right)^{\gamma_1}\frac{B^2}{\langle\delta B^2\rangle} = \kappa_{03}\frac{w}{c}\left(\frac{P_b}{P_0}\right)^{\gamma_1}\left(\frac{P_O}{P_b}\right)^{\gamma_2}\frac{B^2}{\langle\delta B^2\rangle}, \quad \text{(A8)}$$

$$\left(\frac{P_O}{P_{He}}\right) = \left[\left(\frac{A_O}{A_{He}}\right)\left(\frac{P_O}{P_b}\right)^{(\gamma_1-\gamma_2)}\right]^{1/(1+\gamma_1)}. \quad \text{(A9)}$$

Next, for the region $P_O \geqslant P_t$

$$\kappa_{03}\frac{w}{c}\left(\frac{P_b}{P_0}\right)^{\gamma_1}\left(\frac{P_{He}}{P_b}\right)^{\gamma_2}\frac{B^2}{\langle\delta B^2\rangle} = \kappa_{03}\frac{w}{c}\left(\frac{P_b}{P_0}\right)^{\gamma_1}\left(\frac{P_O}{P_b}\right)^{\gamma_2}\frac{B^2}{\langle\delta B^2\rangle}, \quad \text{(A10)}$$

$$\left(\frac{P_O}{P_{He}}\right) = \left(\frac{A_O}{A_{He}}\right)^{1/(1+\gamma_2)}. \quad \text{(A11)}$$

Finally, the rigidity value P_t can be found by equating Equation (A9) with (A11) at $P_O = P_t$:

$$\left[\left(\frac{A_O}{A_{He}}\right)\left(\frac{P_t}{P_b}\right)^{(\gamma_1-\gamma_2)}\right]^{1/(1+\gamma_1)} = \left(\frac{A_O}{A_{He}}\right)^{1/(1+\gamma_2)}, \quad \text{(A12)}$$

$$P_t = P_b\left(\frac{A_O}{A_{He}}\right)^{1/(1+\gamma_2)}. \quad \text{(A13)}$$

The ratio for the entire rigidity ranges can be expressed as follows:

$$\left(\frac{P_O}{P_{He}}\right) = \begin{cases} \left(\frac{A_O}{A_{He}}\right)^{1/(1+\gamma_1)} & ; P_O \leqslant P_b \\ \left[\left(\frac{A_O}{A_{He}}\right)\left(\frac{P_O}{P_b}\right)^{(\gamma_1-\gamma_2)}\right]^{1/(1+\gamma_1)} & ; P_b \leqslant P_O \leqslant P_t \\ \left(\frac{A_O}{A_{He}}\right)^{1/(1+\gamma_2)} & ; P_O \geqslant P_t, \end{cases} \quad \text{(A14)}$$

where $P_t = P_b\left(\frac{A_O}{A_{He}}\right)^{1/(1+\gamma_2)}$.

REFERENCES

Abraham-Shrauner, B. 1972, JGR, 77, 736
Adhikari, L., Zank, G. P., Hu, Q., & Dosch, A. 2014, ApJ, 793, 52
Beck, J. G., & Giles, P. 2005, ApJL, 621, L153
Bell, A. R. 1978, MNRAS, 182, 147
Blandford, R. D., & Ostriker, J. P. 1978, ApJL, 221, L29
Borovikov, S. N., Pogorelov, N. V., Burlaga, L. F., & Richardson, J. D. 2011, ApJL, 728, L21
Breech, B., Matthaeus, W. H., Minnie, J., et al. 2008, JGRA, 113, 8105
Burlaga, L. F., Ness, N. F., Acuña, M. H., et al. 2009, ApJ, 692, 1125
Cummings, A. C. 2011, Proc. 32nd ICRC (Beijing), 11, 2
Cummings, A. C., & Stone, E. C. 2001, ICRC, 10, 4243
Cummings, A. C., & Stone, E. C. 2003, ICRC, 7, 3897
Cummings, A. C., & Stone, E. C. 2008, ICRC, 1, 827
Cummings, A. C., Stone, E. C., & Steenberg, C. D. 2002, ApJ, 578, 194
Cummings, A. C., Stone, E. C., & Webber, W. R. 1984, ApJL, 287, L99
Decker, R. B., Krimigis, S. M., Roelof, E. C., et al. 2008, Natur, 454, 67
Drake, J. F., Opher, M., Swisdak, M., & Chamoun, J. N. 2010, ApJ, 709, 963
Ebert, R. W., McComas, D. J., Elliott, H. A., Forsyth, R. J., & Gosling, J. T. 2009, JGRA, 114, 1109
Fisk, L. A., & Gloeckler, G. 2009, AdSpR, 43, 1471
Florinski, V., Guo, X., Balsara, D. S., & Meyer, C. 2013, ApJS, 205, 19
Florinski, V., & Pogorelov, N. V. 2009, ApJ, 701, 642
Giacalone, J., & Decker, R. 2010, ApJ, 710, 91
Giacalone, J., Jokipii, J. R., & Kota, J. 1994, JGR, 99, 19351

Guo, F., Jokipii, J. R., & Kota, J. 2010, ApJ, 725, 128
Gurnett, D. A., Kurth, W. S., Burlaga, L. F., & Ness, N. F. 2013, Sci, 341, 1489
Hill, M. E., Hamilton, D. C., & Krimigis, S. M. 2002, ApJL, 572, L169
Isenberg, P. A., Smith, C. W., Matthaeus, W. H., & Richardson, J. D. 2010, ApJ, 719, 716
Jian, L. K., Russell, C. T., & Luhmann, J. G. 2011, SoPh, 274, 321
Jokipii, J. R. 1966, ApJ, 146, 480
Jokipii, J. R. 1971, RvGSP, 9, 27
Jokipii, J. R. 1996, ApJL, 466, L47
Kóta, J. 2010, ApJ, 723, 393
Kóta, J., & Jokipii, J. R. 2008, in AIP Conf. Ser. 1039, Particle Acceleration and Transport in the Heliosphere and Beyond, ed. G. Li et al. (Melville, NY: AIP), 397
Krimigis, S. M., Decker, R. B., Roelof, E. C., et al. 2013, Sci, 341, 144
Krymskii, G. F. 1977, DoSSR, 234, 1306
Lallement, R., Quémerais, E., Bertaux, J. L., et al. 2005, Sci, 307, 1447
Lazarian, A., & Opher, M. 2009, ApJ, 703, 8
le Roux, J. A. 2011, ApJ, 743, 72
le Roux, J. A., Webb, G. M., Florinski, V., & Zank, G. P. 2007, ApJ, 662, 350
le Roux, J. A., Zank, G. P., & Ptuskin, V. S. 1999, JGR, 104, 24845
Li, H., Wang, C., & Richardson, J. D. 2008, GeoRL, 35, 19107
McComas, D. J., Alexashov, D., Bzowski, M., et al. 2012, Sci, 336, 1291
McComas, D. J., & Schwadron, N. A. 2006, GeoRL, 33, 4102
Mewaldt, R. A., Selesnick, R. S., Cummings, J. R., Stone, E. C., & von Rosenvinge, T. T. 1996, ApJL, 466, L43
Opher, M., Stone, E. C., & Liewer, P. C. 2006, ApJL, 640, L71
Parker, E. N. 1958, ApJ, 128, 664
Parker, E. N. 1960, ApJ, 132, 821
Parker, E. N. 1965, P&SS, 13, 9
Pesses, M. E., Eichler, D., & Jokipii, J. R. 1981, ApJL, 246, L85
Pogorelov, N. V., Stone, E. C., Florinski, V., & Zank, G. P. 2007, ApJ, 668, 611
Pogorelov, N. V., Zank, G. P., & Ogino, T. 2004, ApJ, 614, 1007
Rucinski, D., Bzowski, M., & Fahr, H. J. 2003, AnGp, 21, 1315
Russell, C. T., Jian, L. K., & Luhmann, J. G. 2013, JAdR, 4, 253
Scherer, K., & Fahr, H.-J. 2009, A&A, 495, 631
Schwadron, N. A., & McComas, D. J. 2003, GeoRL, 30, 1587
Schwadron, N. A., Zurbuchen, T. H., Fisk, L. A., & Gloeckler, G. 1999, JGR, 104, 535
Senanayake, U. K., & Florinski, V. 2013, ApJ, 778, 122
Stone, E. C., Cummings, A. C., McDonald, F. B., et al. 2005, Sci, 309, 2017
Stone, E. C., Cummings, A. C., McDonald, F. B., et al. 2008, Natur, 454, 71
Stone, E. C., Cummings, A. C., McDonald, F. B., et al. 2013, Sci, 341, 150
Stone, E. C., Vogt, R. E., McDonald, F. B., et al. 1977, SSRv, 21, 355
Usmanov, A. V., Matthaeus, W. H., Breech, B. A., & Goldstein, M. L. 2011, ApJ, 727, 84
Webber, W., & McDonald, F. 2013, GeoRL, 40, 1665
Wicks, R. T., Chapman, S. C., & Dendy, R. O. 2009, ApJ, 690, 734
Wicks, R. T., Owens, M. J., & Horbury, T. S. 2010, SoPh, 262, 191
Zank, G. 1999, ICRC, 7, 468
Zank, G. P., Li, G., Florinski, V., et al. 2006, JGRA, 111, 6108
Zank, G. P., & Müller, H.-R. 2003, JGRA, 108, 1240